Strong-coupling charge density wave in a one-dimensional topological metal

Philip Hofmann,[1,*] Miguel M. Ugeda,[2,3] Anton Tamtögl,[4] Adrian Ruckhofer,[4] Wolfgang E. Ernst,[4] Giorgio Benedek,[2,5] Antonio J. Martínez-Galera,[6] Anna Stróżecka,[7] José M. Gómez-Rodríguez,[6,8,9] Emile Rienks,[1] Maria Fuglsang Jensen,[1] José I. Pascual,[10,3] and Justin W. Wells[11]

[1]*Department of Physics and Astronomy, Interdisciplinary Nanoscience Center (iNANO), Aarhus University, 8000 Aarhus C, Denmark*
[2]*Donostia International Physics Center, DIPC, 20018 San Sebastian-Donostia, Spain*
[3]*Ikerbasque, Basque Foundation for Science, 48011 Bilbao, Spain*
[4]*Institute of Experimental Physics, Graz University of Technology, 8010 Graz, Austria*
[5]*Dipartimento di Scienza dei Materiali, Universitá di Milano-Bicocca, Via Roberto Cozzi 55, 20125 Milano, Italy*
[6]*Department Física de la Materia Condensada, Universidad Autónoma de Madrid, Madrid 28049, Spain*
[7]*Institut für Experimentalphysik, Freie Universität Berlin, 14195 Berlin, Germany*
[8]*Instituto Nicolas Cabrera, Universidad Autónoma de Madrid, 28049 Madrid, Spain*
[9]*Condensed Matter Physics Center (IFIMAC), Universidad Autónoma de Madrid, 28049 Madrid, Spain*
[10]*CIC nanoGUNE, 20018 San Sebastián-Donostia, Spain*
[11]*Department of Physics, Center for Quantum Spintronics, Norwegian University of Science and Technology, NO-7491 Trondheim, Norway*

(Received 12 July 2017; published 25 January 2019)

Scanning tunneling microscopy, low-energy electron diffraction, and helium atom scattering show a transition to a dimerizationlike reconstruction in the one-dimensional atomic chains on Bi(114) at low temperatures. One-dimensional metals are generally unstable against such a Peierls-like distortion, but neither the shape nor the spin texture of the Bi(114) Fermi contour favors the transition: Although the Fermi contour is one dimensional and thus perfectly nested, the very short nesting vector $2k_F$ is inconsistent with the periodicity of the distortion. Moreover, the nesting occurs between two Fermi contour branches of opposite spin, which is also expected to prevent the formation of a Peierls phase. Indeed, angle-resolved photoemission spectroscopy does not reveal any change in the electronic structure near the Fermi energy around the phase transition. On the other hand, distinct changes at higher binding energies are found to accompany the structural phase transition. This suggests that the transition of a strong-coupling type and that it is driven by phonon entropy rather than electronic entropy. This picture is supported by the observed short correlation length of the pairing distortion, the second-order-like character of the phase transition, and pronounced differences between the surface phonon spectra of the high- and low-temperature phases.

DOI: 10.1103/PhysRevB.99.035438

I. INTRODUCTION

The experimental realization of systems with reduced dimensions has often been the key to the discovery of fundamentally new physics. Of particular importance is the situation in one dimension (1D) with its drastically enhanced significance of electronic correlations and electron-phonon coupling [1,2]. An attractive path to studying systems of reduced dimensionality is to create them on the surfaces of semiconducting or semimetallic substrates as this opens the possibility to employ powerful spectroscopic techniques, such as scanning tunneling microscopy (STM), angle-resolved photoemission (ARPES), and surface-sensitive transport measurements [3,4]. Many systems have been realized and studied in this way, such as metallic chains or graphene nanoribbons on semiconductors, see, e.g., Refs. [5–11].

A particularly intriguing situation arises when low dimensionality is combined with an unconventional spin texture of the electronic states as this imposes a number of restrictions on the allowed electronic instabilities [8,12]. This combination is realized on the (114) [13,14] and (441) [15] vicinal surfaces of Bi where strongly Rashba-split surface states span the gap of a semimetallic substrate. Moreover, due to the similarity of Bi to the topological insulator $Bi_{1-x}Sb_x$ [16,17], all Bi surfaces have metallic surface states with a spin texture similar to that of topological insulators [18,19] and several hallmark features of these states, such as the lack of backscattering [20], were first observed on Bi surfaces. It was also pointed out that a Fermi contour with a chiral spin texture should not lead to charge density wave (CDW) formation even in the presence of perfect nesting [12].

The fundamental difference between a conventional one-dimensional metal at half-filling and the electronic surface state on Bi(114) is illustrated in Fig. 1. A conventional electronic state in a lattice with spacing a and half-filling is unstable with respect to the formation of a one-dimensional CDW also called a Peierls distortion. Figure 1(a) illustrates this situation of ideal nesting with a nesting vector length of $2k_F = \pi/a$ as indicated by the arrow in Fig. 1(a). As this corresponds to a real-space periodicity of $2a$, a Peierls-type distortion involving a periodicity doubling via pairing of the

*philip@phys.au.dk

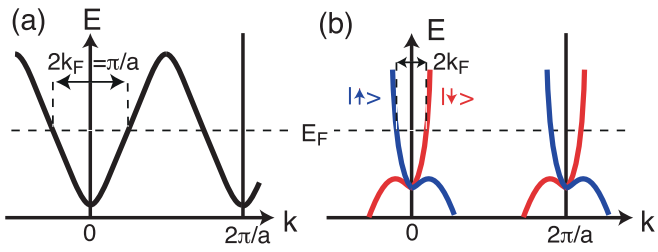

FIG. 1. (a) Conventional one-dimensional electronic state at half-filling. The black dispersion is spin degenerate. This system is sensitive to a Peierls-type instability due to the perfect nesting and the fact that the nesting vector's length corresponds to a real-space periodicity of $2a$. (b) Situation on Bi(114). The spin degeneracy of the bands is lifted, and although perfect nesting is still present, it takes place for a very short nesting vector and between states of opposite spin (indicated by the color of the bands and the arrows), thus protecting against a Peierls-type instability.

atoms in a chain leads to a new Brillouin zone boundary at the Fermi-level crossings of the unreconstructed phase, a gap opening, and hence to an electronic energy gain in the occupied states. The situation is quite different for the surface state on Bi(114) shown in Fig. 1(b). Here, the state is no longer spin degenerate, and the spin texture (indicated by red and blue) and dispersion closely resemble that of a one-dimensional edge state of a two-dimensional topological insulator, the so-called quantum spin Hall effect [21–24]. It is for this reason that Bi(114) has been called a "one-dimensional topological metal" [13]. Although perfect nesting is retained, as for any one-dimensional structure, $2k_F \ll \pi/a$ and a pairing-type reconstruction would not be expected to open a gap at the Fermi-level crossing. More importantly, the spin texture prevents the singularity in the electronic susceptibility required to drive the instability [12], an effect closely related to the forbidden backscattering for such a one-dimensional state [20]. A Peierls distortion would thus not be expected for the case of Bi(114).

Surprisingly, as we report here, such a pairing distortion is nevertheless observed at low temperature on the quasi-one-dimensional Bi(114) surface. Temperature-dependent measurements of the electronic structure by ARPES do not show any signs of a Fermi-surface change as expected from the arguments above but do show some clear spectral changes at higher binding energy. STM, low-energy electron diffraction (LEED), and helium atom scattering (HAS), on the other hand, provide evidence that this transition is a strong-coupling CDW [25], driven by phonon entropy. Strong-coupling CDWs that are not based on Fermi-surface nesting are common for two-dimensional CDW systems [25–31], consistent with strong sensitivity of the electronic susceptibility towards small deviations from ideal nesting conditions [32]. In one dimension, there is always perfect nesting, but in the present case, the nested Fermi surface is irrelevant for the phase transition.

II. EXPERIMENTAL DETAILS

The Bi(114) surface was cleaned by sputtering with noble gas ions and annealing between 300 and 400 K. STM measurements were performed both at a fixed temperature (5 K) and at variable temperatures between 40 and 300 K in two different setups. LEED and ARPES data were collected on the SGM-3 end station of ASTRID [33] between 50 and 300 K. The energy resolution varied between 25 meV for the measurements at low photon energies and 65 meV for the large-scale Fermi-surface maps collected with high photon energies. The angular resolution was better than 0.2°. For the HAS measurements, a nearly monochromatic beam of He ($\Delta E/E \approx 2\%$) was scattered off the sample surface in a fixed 91.5° source-sample-detector geometry. Energy dispersive measurements for inelastic scattering were performed using a time-of-flight (TOF) technique with a pseudorandom chopper disk [34]. The momentum transfer parallel to the surface was calculated from the kinematic scattering conditions [35].

III. RESULTS AND DISCUSSION

The atomic structure of Bi(114) consists of parallel atomic rows with an interatomic spacing of 4.54 Å along the rows [13]. A unit cell comprises several of these rows at different heights, and the periodicity of the unreconstructed surface perpendicular to the rows is 14.20 Å. For the clean surface, a reconstruction-induced doubling of this periodicity has been reported [13] such that the actual periodicity perpendicular to the rows is twice this value. Figure 2(a) shows a closeup STM image of the surface at 5 K. Due to the strong corrugation, the periodicity of 28.40 Å perpendicular to the atomic rows is immediately visible. On close inspection, it becomes clear that the periodicity along the rows is also doubled, i.e., the atoms in the rows are not equally spaced, but most of them appear dimerized. A few of these dimers are emphasized in the figure by red frames. This reconstruction does not only affect the atoms in the top row, but also those in deeper-lying rows. The average interatomic distance in the dimers is 4.15 ± 0.1 Å, thus corresponding to $\sim$0.2 Å atomic displacement from the equilibrium position. This is a substantial fraction of the equilibrium spacing, larger than typically found in Peierls systems [37]. Although dimerization is dominant on a short length scale, long-range ordering is poor. Indeed, defects, such as trimers, are found every few dimers in the row (also indicated by a blue frame in the figure). Moreover, the dimerization appears to be a strongly local phenomenon within each row as no correlations between dimer positions in neighboring atomic rows are evident.

We explored the temperature dependence of the dimerization along the atomic rows. Figures 2(b) and 2(c) compare STM images and height profiles measured at increasing temperatures. Although at 40 K the dimerization is still fully intact, at 150 K it starts vanishing and is nearly absent at 195 K with the exception of the immediate vicinity of structural defects (indicated by an arrow) that appear to serve as a seed for the dimerization. Thus, the dimerization is a low-temperature phase with an apparent transition temperature somewhere between 150 and 195 K.

The reconstruction is also observable in diffraction experiments, even though the coherence length is very short as seen from the STM data. Figure 3 shows LEED data taken at 250 and 55 K, i.e., well above and below the transition temperature range determined by STM. The LEED patterns consist of well-separated rows of closely placed sharp spots.

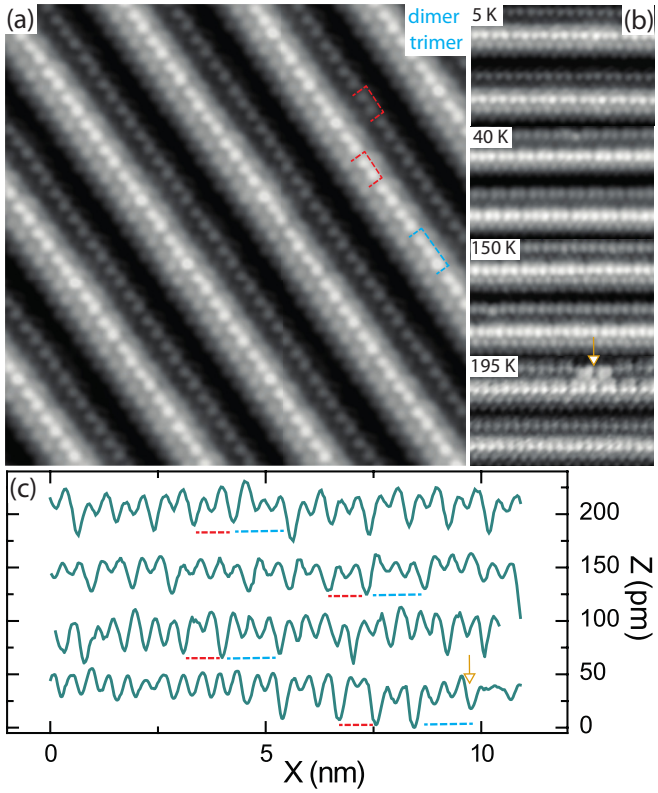

FIG. 2. Dimerization distortion of the quasi-one-dimensional lattice structure of Bi(114). (a) STM image taken at 5 K showing dimer formation in some of the protruding atomic rows (red dashed frames) with frequently appearing defects, such as trimers (blue dashed frame). (b) STM images at higher temperatures and (c) profiles along the protruding atomic rows, measured at the indicated temperatures. At 195 K, the dimerization is lifted and only observed in the immediate vicinity of defects. Tunneling parameters: (a) $U = 0.2$ V and $I = 0.1$ nA and (b) $U = 0.2,\ 1.0,\ -0.1,\ 0.25$ V and $I = 0.1,\ 4.0,\ 2.0,\ 4.0$ nA. All STM data were processed with the WSXM software [36].

The distance between the spots along the rows corresponds to the reciprocal lattice distance perpendicular to the chains ($2\pi/28.4$ Å^{-1}), whereas the distance between the rows corresponds to the interatomic distance in the (unreconstructed)

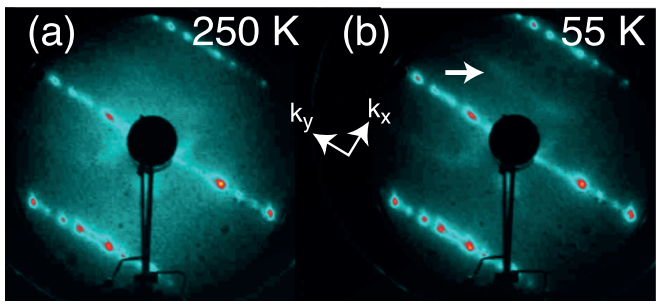

FIG. 3. (a) and (b) LEED patterns collected above and below, respectively, the temperature of the phase transition observed by STM. The arrow in (b) shows the additional streaks induced by the periodicity doubling along the atomic chains. The electron kinetic energy is 27.2 eV.

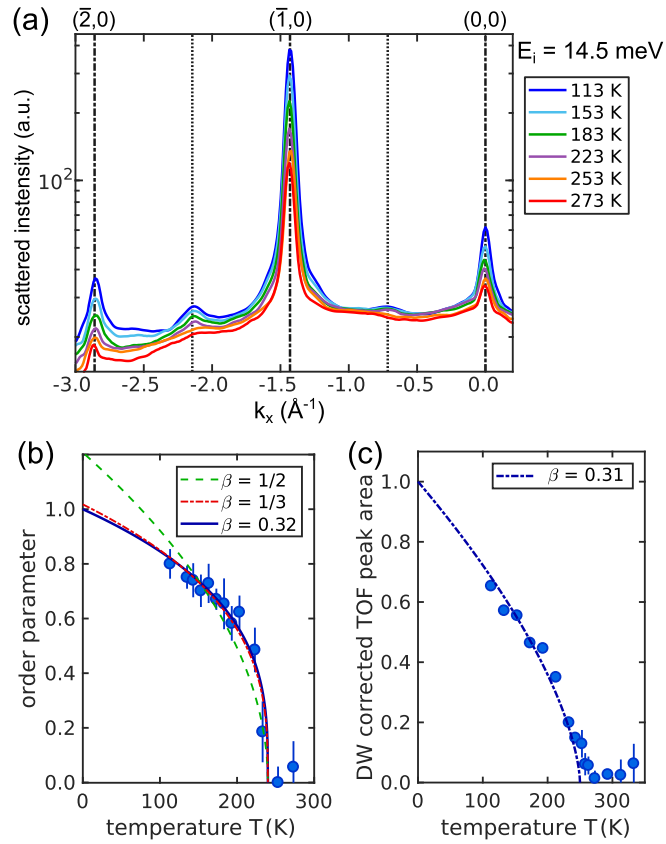

FIG. 4. (a) Scattered He intensities (logarithmic scale) versus parallel momentum transfer k_x (crystal azimuth aligned along $\overline{\Gamma} - \overline{X}$) for various sample temperatures T. A small vertical offset between the individual scans was added for better visibility. The vertical dotted lines illustrate the position of the CDW superlattice peaks due to the doubled periodicity. (b) Normalized square root of the CDW superlattice peak's integrated intensity (peak at $k_x = -2.15$ Å^{-1}), which is proportional to the CDW order parameter. The lines represents fits to Eq. (1) for different choices of the critical exponent β. (c) Peak area of the CDW superlattice peak when integrated over energy in the energy-resolved TOF measurements.

chains ($2\pi/4.54$ Å^{-1}). In the low-temperature image, weak streaks of intensity are observed halfway between the rows (indicated by an arrow) (see the Supplemental Material [38]) and thus consistent with a dimerized structure. The width of streaks along k_x reflects the short coherence of the CDW within the atomic rows, and the (much larger) width along k_y is due to the lack of coherence between these rows. These findings are consistent with the STM results.

A more detailed picture of the phase transition is provided by HAS. Figure 4(a) displays the scattered He intensity versus momentum transfer k_x for various sample temperatures T using an incident beam energy E_i of 14.5 meV. At low temperatures, a small enhancement of the scattered intensity appears halfway between the diffraction peaks which is consistent with a superstructure based on a doubled periodicity along the rows as observed by the LEED and STM measurements. Scans with different beam energies show that this cannot be due to any resonance effect and is indeed caused by a reconstruction [39].

Figure 4(b) shows the temperature dependence of the square root of the integrated intensity for the CDW superlattice peak halfway between the $(\bar{2}, 0)$ and the $(\bar{1}, 0)$ Bragg peaks [see Fig. 4(a)]. In order to access the intensity change relevant to the critical fluctuations of the CDW [40,41] as opposed to the intensity changes due to the Debye-Waller factor [42], the integrated intensity $I(T)$ shown in the figure has been normalized to that of the specular beam (see the Supplemental Material [38]) for more details on the procedure). This correction is particularly necessary in view of the low surface Debye temperature of Bi ($\Theta_D = 85$ K $< T_c$ [43,44], where T_c is the CDW transition temperature). The square root of the resulting $I(T)$ can then be viewed as the order parameter of the CDW [45,46]. $I(T)$ shows a sharp onset below approximately 250 K, followed by a continuous rise at lower temperatures.

The temperature dependence of the order parameter $\sqrt{I(T)}$ can be used to determine T_c and the critical exponent β belonging to the phase transition [40,41,47–49]. This is achieved by fitting the power law,

$$\sqrt{\frac{I(T)}{I(0)}} = \left(1 - \frac{T}{T_c}\right)^{\beta} \tag{1}$$

to the data in Fig. 4(b) [$I(0)$ is the extrapolated intensity at 0 K], resulting in $T_c = (242 \pm 7)$ K and $\beta = (0.32 \pm 0.02)$. The fit is represented by the blue solid line in Fig. 4(b).

Our finding of $\beta = (0.32 \pm 0.03)$ is very close to the universal exponent of 1/3 as predicted in the presence of fluctuations [49], in agreement with the findings of other CDWs in layered chalcogenides and quasi-1D systems [41,50–53]. On the other hand, using mean-field theory where fluctuations are neglected ($\beta = 1/2$), results in the green dashed curve which does not represent a satisfactory fit to the data. When fitting the data under the constraint that $\beta = 1/3$, we obtain the red dashed curve in Fig. 4(b) and a transition temperature of $T_c = (245 \pm 8)$ K.

At first glance, the transition temperature determined from HAS appears to be inconsistent with the STM data that does not show any short-range order above 195 K. We must keep in mind, however, that strong fluctuations are to be expected and that STM, being a slow technique, only measures the *average* position of the atomic motion and might thus not be able to show the preserved local dimerization at high temperatures. This actually explains why close to defects, dimerization can still be observed frozen in the 195-K images. Indeed, LEED patterns taken at 200 and even 250 K do still show very weak signatures of the superstructure {see Fig. 3(a) and the Supplemental Material [38]}.

Energy-resolved scans performed at the position of the CDW superlattice peak confirm that the enhanced elastic intensity is indeed due to a static change in the structure and cannot be caused by any inelastic effects, such as kinematical focusing [39]. Figure 4(c) shows the TOF peak intensity versus surface temperature which was obtained by fitting the energy-resolved scans with a single Gaussian and applying a correction for the Debye-Waller attenuation (for the original TOF data, see the Supplemental Material [38]). The temperature range where the peak intensity shows a strong rise is consistent with T_c as determined from the data in Fig. 4(b),

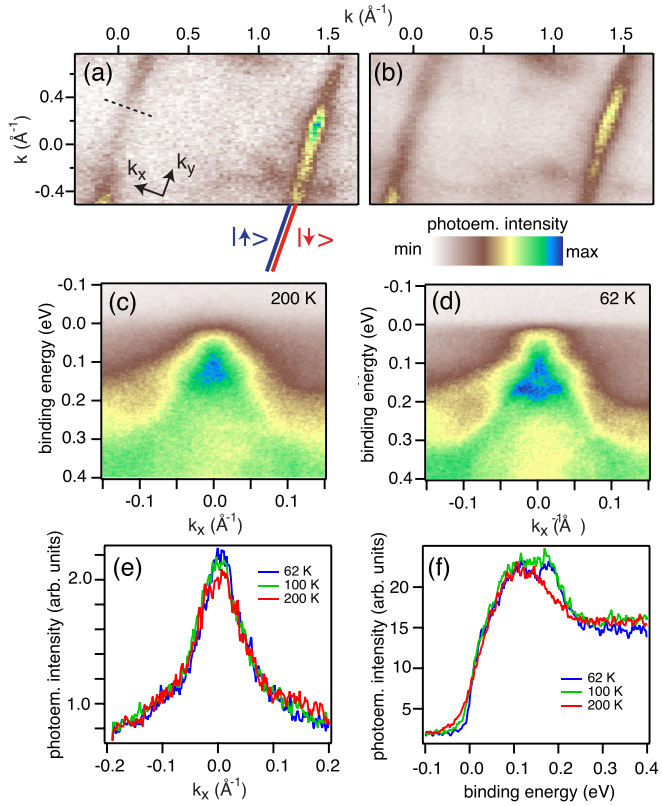

FIG. 5. (a) and (b) Photoemission intensity in the low-temperature phase at $T = 60$ K in a 20-meV window around the Fermi energy and a binding energy of 170 meV, respectively. The sketched continuation of the Fermi surface illustrates that the observed linelike intensity is composed of two unresolved spin-polarized Fermi-level crossings [13], see also Fig. 1(b). The photon energy is $h\nu = 70$ eV. The dashed line shows the direction of the data in (c) and (e). (c) and (d) Photoemission intensity close to and below the CDW transition (at $T = 200$ and 62 K), respectively, along the dashed black line in (a). (e) Momentum distribution curves at the Fermi energy along the dashed line in (a) as a function of temperature. (f) Energy distribution curves along the crossing point of the dashed line in (a) and the Fermi surface at $k_x = 0$, i.e., through the center of the images in (c) and (d). $h\nu = 17$ eV in (c)–(f).

and fitting a critical exponent gives rise to $\beta = (0.31 \pm 0.04)$, also consistent with the data in Fig. 4(b).

After characterizing the phase transition using structural techniques, we now move to the spectroscopic characterization of the electronic and vibrational states by ARPES and HAS. Figure 5(a) shows the $k_{\parallel}$-dependent photoemission intensity at the Fermi level at 60 K. It is dominated by intense lines in the direction perpendicular to the atomic rows. As has been shown by spin-resolved photoemission, these intense lines are actually caused by the two unresolved spin-polarized Fermi-surface elements due to the spin-split surface state in Fig. 1(b) [13]. This unresolved Fermi contour is indicated as a sketch, extending the observed Fermi contour in the figure. Apart from the intense linear features, the photoemission intensity shows some weak structures that can be assigned to bulk states. A projection of the (small) bulk Fermi surface of Bi onto the (114) surface is given in Ref. [13].

Since the Fermi surface of Fig. 5(a) is measured in the dimerized phase, one might expect replicas of the Fermi-surface lines in between the two intense lines, similar to the additional weak streaks in between the lines of densely spaced spots in the LEED image of Fig. 3(b). Such replicas are not observed, neither at the Fermi surface in Fig. 5(a) nor for the higher binding energy of 170 meV in Fig. 5(b). Note that the lack of replica bands in a CDW is also found for many two-dimensional CDW systems where the spectral weight in the CDW phase tracks that of the normal phase [27]. Hence the CDW period observed in direct space may not correspond to nesting, i.e., to the $2k_F$ measured with high-resolution ARPES in reciprocal space.

Figures 5(c) and 5(d) show the electronic structure of the one-dimensional states above and below, respectively, the dimerization transition temperature as a function of binding energy in the k_x direction perpendicular to the one-dimensional Fermi surface along a cut indicated by the black dashed line in Fig. 5(a). No spectroscopic signature of the transition is observed near the Fermi energy. Indeed, when taking momentum distribution curves (MDCs) through a temperature-dependent series of similar data sets, no significant changes can be observed [see Fig. 5(e)] except for a minor sharpening of the MDC peak at low temperatures as expected due to electron-phonon coupling [54,55].

However, there is a significant change in the electronic structure rather far away from the Fermi energy at around 150 meV where a single intense feature at 110 meV in the high-temperature phase of Fig. 5(c) splits into two peaks, one essentially staying at the same binding energy and one moving to a higher energy of 175 meV. This spectral change is especially well seen in energy distribution curves through the center of a series of temperature-dependent data (see the Supplemental Material [38]) shown in Fig. 5(f). These changes in the electronic structure at high binding energy do not lead to observable replicas in the constant energy surfaces either as seen in Fig. 5(b) which shows the photoemission intensity at a binding energy of 170 meV.

The observation of spectral changes only at high binding energy rules out that the transition is due to a nesting-driven weak CDW, such as the Peierls distortion in Fig. 1(b), as this would require a gap opening at the Fermi energy. On the other hand, an electronic structure change in which states are shifted to a substantially higher binding energy can certainly explain the stabilization of the reconstructed phase. This gives a qualitative explanation for the stability of the pairing distortion at low temperatures, but it does not explain why the pairing should be lifted at higher temperatures. In a conventional Peierls scenario, the transition from the CDW state to the normal state is driven by electronic entropy when the thermal energy becomes comparable to the gap energy. This cannot be the case here. We also note that the CDW is unlikely to be caused by bulk states because of the extremely small density of bulk states at E_F and because of the absence of a CDW in bulk Bi.

A plausible alternative scenario is that the transition is a strong-coupling CDW, driven by phonon entropy [25,29,45,56], and this is supported by several experimental facts, such as the short coherence length and considerable atomic displacements observed here. A strong-coupling

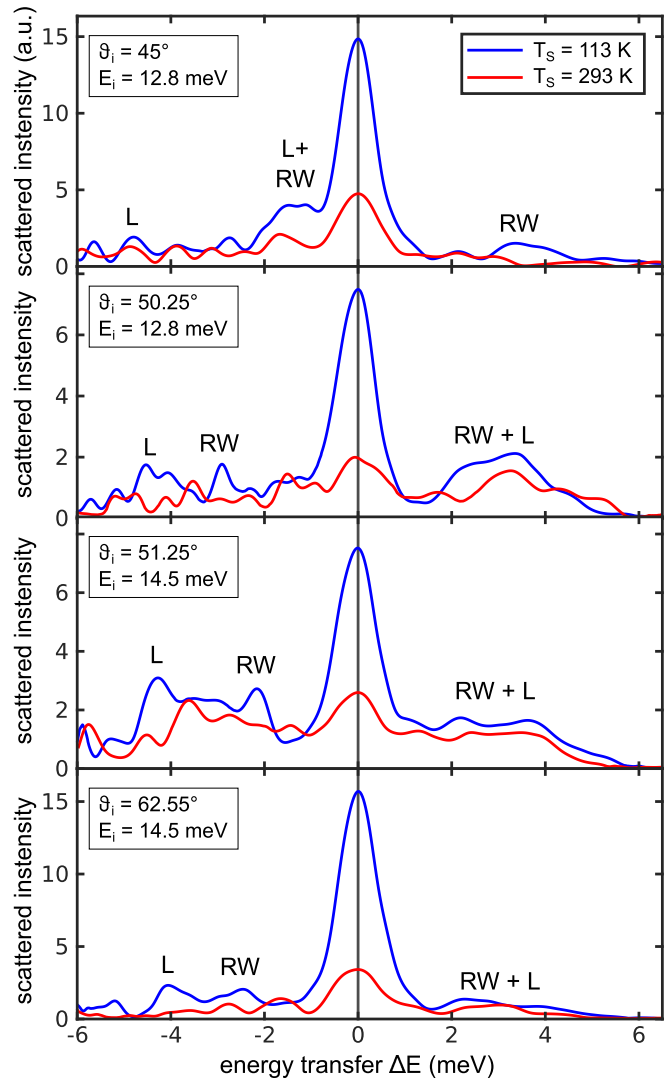

FIG. 6. Comparison of several TOF spectra for the cooled sample and the sample at room temperature, transformed to energy transfer spectra $\Delta E = E_f - E_i$. Energy loss ($\Delta E < 0$) corresponds to the creation of a phonon with phonon energy $\Delta E = \hbar\omega$, and energy gain ($\Delta E > 0$) corresponds to the annihilation of a phonon. RW and L stand for the Rayleigh wave and longitudinal phonon modes, respectively.

CDW would not be uncommon for a one-dimensional surface structure. A similar mechanism has also been suggested for the CDW of In nanowires on Si(111) [57] which, however, also shows a pronounced gap opening at the Fermi energy [5,58]. Most importantly, the strong-coupling picture would explain why a temperature-dependent distortion can appear in a system with this particular spin texture for which it would otherwise not be expected.

A phonon entropy driven phase transition typically gives rise to a change in the phonon density of states, as recently observed for the metal insulator transition in VO_2 [56]. HAS can, in principle, be used to map the full surface phonon dispersion and is especially valuable because its high resolution gives access to low-energy phonons. In the case of Bi(114), the cross section for inelastic phonon scattering turned out to be extremely small such that only spectra at a few values

of the momentum transfer could be measured. TOF spectra were recorded along the $\overline{\Gamma} - \overline{X}$ azimuth with the sample at room temperature and $T = 113$ K. The TOF spectra were then transformed to energy transfer spectra which allows inelastic- (phonon) scattering events to be determined. The energy transfer $\Delta E = E_f - E_i$ was determined by the initial energy E_i, and final energy E_f of the helium atom, energy loss ($\Delta E < 0$), and gain peaks ($\Delta E > 0$) correspond to the creation and annihilation of a phonon, respectively [35].

Figure 6 gives a selection of inelastic spectra measured at different incident energies and angles. The most prominent inelastic features are labeled as RW and L, based on the experimentally and theoretically determined surface phonon dispersion of Bi(111) along $\overline{\Gamma} - \overline{M}$ [35]. Although the data do not give the full surface phonon dispersion, two important conclusions can be drawn: First, we observe a significant change in the phonon spectrum between the two phases. Although the Jacobian scaling upon transforming from TOF to energy transfer increases the height of the experimental noise on the phonon creation side of the spectrum ($\Delta E < 0$), this can be clearly seen on the loss side by comparing the most pronounced peaks at the two temperatures. Second, the low-temperature phase generally shows more intense features on the gain side (phonon annihilation) of the elastic peak, consistent with a higher phonon occupation in the low-temperature phase. Since the Bose factor for the low-energy acoustic modes is not substantially different between both temperatures, it indicates that the phonon density of states changes below T_c. Hence the observation of an enhanced intensity of the low-energy acoustic surface phonon modes below T_c is in line with a strong phonon contribution to the transition entropy.

IV. CONCLUSION

In conclusion, we have reported the observation of a dimerization transition below (245 ± 8) K on Bi(114). Such a transition is highly unexpected even in the presence of a perfectly nested one-dimensional Fermi contour because it appears to be forbidden by the spin texture of the states and the nonmatching nesting vector $2k_F$. Indeed, the transition does not involve the states near the Fermi energy, but spectral changes at higher binding energy are observed. This, as well as the short coherence length and significant changes in the phonon spectrum, support the interpretation of the low-temperature state as a strong-coupling CDW, illustrating that such transitions are still possible in topological systems.

More detailed insight into the driving force of the phase transition could, in principle, be gained by first-principles calculations of the electronic structure, vibrational properties, and electron-phonon coupling in the system, similar to the work that has been carried out for In on Si(111) [57]. In the present case, such calculations are extremely challenging due to the large unit cell, the need to include the spin-orbit interaction for an adequate description of the electronic states and the need for a thick slab in the calculation in order to decouple the deeply penetrating surface states. However, such calculations could give unprecedented insight into role of the spin-split surface states (if any) in a surface CDW of a topological material.

ACKNOWLEDGMENTS

We gratefully acknowledge stimulating discussions with K. Rossnagel, M. Hengsberger, and J. Osterwalder. This work was supported by the Danish Council for Independent Research, Natural Sciences under the Sapere Aude Program (Grant No. DFF-4002-00029) and by VILLUM FONDEN via the center of Excellence for Dirac Materials (Grant No. 11744). J.W.W. acknowledges support from the Institute for Storage Ring Facilities, Aarhus University during the beam time for this project and from the Research Council of Norway through its Centres of Excellence funding scheme, Project No. 262633 "QuSpin" as well as via the Fripro Program, Project No. 250985 "FunTopoMat." A.J.M.-G. acknowledges funding from the Spanish MINECO through the Juan de la Cierva Program (ref. IJCI-2014-19209). J.M.G.-R acknowledges financial support from the Spanish MINECO under Project No. MAT2016-77852-C2-2-R. A.T. and W.E.E. acknowledge financial support provided by the FWF (Austrian Science Fund) within Project No. P29641-N36.

[1] R. E. Peierls, *Quantum Theory of Solids* (Oxford University Press, Oxford, 1955).
[2] J. M. Luttinger and J. C. Ward, Phys. Rev. **118**, 1417 (1960).
[3] P. Hofmann and J. W. Wells, J. Phys.: Condens. Matter **21**, 013003 (2009).
[4] J. W. Wells, K. Handrup, J. F. Kallehauge, L. Gammelgaard, P. Boggild, M. B. Balslev, J. E. Hansen, P. R. E. Petersen, and P. Hofmann, J. Appl. Phys. **104**, 053717 (2008).
[5] H. W. Yeom, S. Takeda, E. Rotenberg, I. Matsuda, K. Horikoshi, J. Schaefer, C. M. Lee, S. D. Kevan, T. Ohta, T. Nagao, and S. Hasegawa, Phys. Rev. Lett. **82**, 4898 (1999).
[6] J. N. Crain, A. Kirakosian, K. N. Altmann, C. Bromberger, S. C. Erwin, J. L. McChesney, J. L. Lin, and F. J. Himpsel, Phys. Rev. Lett. **90**, 176805 (2003).
[7] C. Tegenkamp, T. Ohta, J. L. McChesney, H. Dil, E. Rotenberg, H. Pfnur, and K. Horn, Phys. Rev. Lett. **100**, 076802 (2008).
[8] C. Tegenkamp, D. Lükermann, H. Pfnür, B. Slomski, G. Landolt, and J. H. Dil, Phys. Rev. Lett. **109**, 266401 (2012).
[9] J. Park, S. W. Jung, M.-C. Jung, H. Yamane, N. Kosugi, and H. W. Yeom, Phys. Rev. Lett. **110**, 036801 (2013).
[10] J. Baringhaus, M. Ruan, F. Edler, A. Tejeda, M. Sicot, T.-I. Amina, A.-P. Li, Z. Jiang, E. H. Conrad, C. Berger *et al.*, Nature (London) **506**, 349 (2014).
[11] S. Cheon, T.-H. Kim, S.-H. Lee, and H. W. Yeom, Science **350**, 182 (2015).
[12] T. K. Kim, J. Wells, C. Kirkegaard, Z. Li, S. V. Hoffmann, J. E. Gayone, I. Fernandez-Torrente, P. Haberle, J. I. Pascual, K. T. Moore *et al.*, Phys. Rev. B **72**, 085440 (2005).
[13] J. W. Wells, J. H. Dil, F. Meier, J. Lobo-Checa, V. N. Petrov, J. Osterwalder, M. M. Ugeda, I. Fernandez-Torrente, J. I. Pascual, E. D. L. Rienks *et al.*, Phys. Rev. Lett. **102**, 096802 (2009).
[14] D. Leuenberger, H. Yanagisawa, S. Roth, J. H. Dil, J. W. Wells, P. Hofmann, J. Osterwalder, and M. Hengsberger, Phys. Rev. Lett. **110**, 136806 (2013).

[15] M. Bianchi, F. Song, S. Cooil, A. F. Monsen, E. Wahlström, J. A. Miwa, E. D. L. Rienks, D. A. Evans, A. Strozecka, J. I. Pascual *et al.*, Phys. Rev. B **91**, 165307 (2015).

[16] J. C. Y. Teo, L. Fu, and C. L. Kane, Phys. Rev. B **78**, 045426 (2008).

[17] D. Hsieh, D. Qian, L. Wray, Y. Xia, Y. S. Hor, R. J. Cava, and M. Z. Hasan, Nature (London) **452**, 970 (2008).

[18] P. Hofmann, Prog. Surf. Sci. **81**, 191 (2006).

[19] X.-L. Qi and S.-C. Zhang, Rev. Mod. Phys. **83**, 1057 (2011).

[20] J. I. Pascual, G. Bihlmayer, Y. M. Koroteev, H. P. Rust, G. Ceballos, M. Hansmann, K. Horn, E. V. Chulkov, S. Blugel, P. M. Echenique *et al.*, Phys. Rev. Lett. **93**, 196802 (2004).

[21] C. L. Kane and E. J. Mele, Phys. Rev. Lett. **95**, 226801 (2005).

[22] S. Murakami, Phys. Rev. Lett. **97**, 236805 (2006).

[23] B. A. Bernevig and S.-C. Zhang, Phys. Rev. Lett. **96**, 106802 (2006).

[24] M. Konig, S. Wiedmann, C. Brune, A. Roth, H. Buhmann, L. W. Molenkamp, X.-L. Qi, and S.-C. Zhang, Science **318**, 766 (2007).

[25] W. L. McMillan, Phys. Rev. B **16**, 643 (1977).

[26] M. D. Johannes, I. I. Mazin, and C. A. Howells, Phys. Rev. B **73**, 205102 (2006).

[27] K. Rossnagel, J. Phys.: Condens. Matter **23**, 213001 (2011).

[28] M. Calandra, I. I. Mazin, and F. Mauri, Phys. Rev. B **80**, 241108 (2009).

[29] X. Zhu, Y. Cao, J. Zhang, E. W. Plummer, and J. Guo, Proc. Natl. Acad. Sci. **112**, 2367 (2015).

[30] U. Chatterjee, J. Zhao, M. Iavarone, R. Di Capua, J. P. Castellan, G. Karapetrov, C. D. Malliakas, M. G. Kanatzidis, H. Claus, J. P. C. Ruff *et al.*, Nat. Commun. **6**, 6313 (2015).

[31] C.-W. Chen, J. Choe, and E. Morosan, Rep. Prog. Phys. **79**, 084505 (2016).

[32] M. D. Johannes and I. I. Mazin, Phys. Rev. B **77**, 165135 (2008).

[33] S. V. Hoffmann, C. Søndergaard, C. Schultz, Z. Li, and P. Hofmann, Nucl. Instrum. Methods Phys. Res., Sect. A **523**, 441 (2004).

[34] A. Tamtögl, M. Mayrhofer-Reinhartshuber, N. Balak, W. E. Ernst, and K. H. Rieder, J. Phys.: Condens. Matter **22**, 304019 (2010).

[35] A. Tamtögl, P. Kraus, M. Mayrhofer-Reinhartshuber, D. Campi, M. Bernasconi, G. Benedek, and W. E. Ernst, Phys. Rev. B **87**, 035410 (2013).

[36] I. Horcas, R. Fernández, J. M. Gómez-Rodríguez, J. Colchero, J. Gómez-Herrero, and A. M. Baro, Rev. Sci. Instrum. **78**, 013705 (2007).

[37] J.-P. Pouget, C. R. Phys. **17**, 332 (2016); physique de la matière condensée au {XXIe} siècle: l'héritage de Jacques Friedel.

[38] See Supplemental Material at http://link.aps.org/supplemental/10.1103/PhysRevB.99.035438 for LEED and ARPES data taken at different temperatures as well as additional information on the HAS measurement and analysis.

[39] M. Mayrhofer-Reinhartshuber, P. Kraus, A. Tamtögl, S. Miret-Artés, and W. E. Ernst, Phys. Rev. B **88**, 205425 (2013).

[40] S. Girault, A. H. Moudden, and J. P. Pouget, Phys. Rev. B **39**, 4430 (1989).

[41] H. Requardt, M. Kalning, B. Burandt, W. Press, and R. Currat, J. Phys.: Condens. Matter **8**, 2327 (1996).

[42] P. Kraus, A. Tamtögl, M. Mayrhofer-Reinhartshuber, F. Apolloner, C. Gösweiner, S. Miret-Artés, and W. E. Ernst, J. Phys. Chem. C **119**, 17235 (2015).

[43] H. Mönig, J. Sun, Y. M. Koroteev, G. Bihlmayer, J. Wells, E. V. Chulkov, K. Pohl, and P. Hofmann, Phys. Rev. B **72**, 085410 (2005).

[44] M. Mayrhofer-Reinhartshuber, A. Tamtögl, P. Kraus, K. H. Rieder, and W. E. Ernst, J. Phys.: Condens. Matter **24**, 104008 (2012).

[45] G. Grüner, *Density Waves in Solids*, Frontiers in Physics Vol. 89 (Perseus, Cambridge, MA, 1994).

[46] G. Grüner, Rev. Mod. Phys. **60**, 1129 (1988).

[47] H. Nishimori and G. Ortiz, *Elements of Phase Transitions and Critical Phenomena* (Oxford University Press, Oxford, 2010).

[48] R. K. Pathria and P. D. Beale, *Statistical Mechanics*, 3rd ed. (Elsevier, Amsterdam, 2011).

[49] T. Ma and S. Wang, *Phase Transition Dynamics* (Springer, New York, 2014).

[50] G. Brusdeylins, C. Heimlich, J. G. Skofronick, J. P. Toennies, R. Vollmer, and G. Benedek, Europhys. Lett. **9**, 563 (1989).

[51] G. Brusdeylins, C. Heimlich, J. G. Skofronick, J. P. Toennies, R. Vollmer, G. Benedek, and L. Miglio, Phys. Rev. B **41**, 5707 (1990).

[52] J. E. Lorenzo, R. Currat, P. Monceau, B. Hennion, H. Berger, and F. Levy, J. Phys.: Condens. Matter **10**, 5039 (1998).

[53] M. Hoesch, A. Bosak, D. Chernyshov, H. Berger, and M. Krisch, Phys. Rev. Lett. **102**, 086402 (2009).

[54] J. E. Gayone, S. V. Hoffmann, Z. Li, and P. Hofmann, Phys. Rev. Lett. **91**, 127601 (2003).

[55] P. Hofmann, I. Y. Sklyadneva, E. D. L. Rienks, and E. V. Chulkov, New J. Phys. **11**, 125005 (2009).

[56] J. D. Budai, J. Hong, M. E. Manley, E. D. Specht, C. W. Li, J. Z. Tischler, D. L. Abernathy, A. H. Said, B. M. Leu, L. A. Boatner *et al.*, Nature (London) **515**, 535 (2014).

[57] S. Wippermann and W. G. Schmidt, Phys. Rev. Lett. **105**, 126102 (2010).

[58] T. Frigge, B. Hafke, T. Witte, B. Krenzer, C. Streubühr, A. Samad Syed, V. Mikšić Trontl, I. Avigo, P. Zhou, M. Ligges *et al.*, Nature (London) **544**, 207 (2017).